



## Article

# Study of Material Compatibility for a Thermal Energy Storage System with Phase Change Material

Songgang Qiu <sup>1,\*</sup> , Laura Solomon <sup>1</sup>  and Ming Fang <sup>2</sup>

<sup>1</sup> Department of Mechanical and Aerospace Engineering, Benjamin M. Statler College of Engineering and Mineral Resources, West Virginia University, Morgantown, WV 26506, USA; laura.solomon@mail.wvu.edu

<sup>2</sup> Bechtel National Incorporation, Hanford Waste Treatment Plant, Richland, WA 99354, USA; mfang@bechtel.com

\* Correspondence: songgang.qiu@mail.wvu.edu; Tel.: +1-304-293-3342

Received: 21 February 2018; Accepted: 5 March 2018; Published: 6 March 2018

**Abstract:** The suitability of stainless steel 316L and Inconel 625 for use in a latent heat thermal energy storage (TES) system was investigated. A NaCl–NaF eutectic mixture with a melting temperature of 680 °C was used as the phase change material (PCM). Containers were filled with the PCM prior to heating to 750 °C, then examined after 100 and 2500 h of high-temperature exposure by analyzing the material surface and cross-section areas. A small amount of corrosion was present in both samples after 100 h. Neither sample suffered significant damage after 2500 h. The undesirable inter-granular grain boundary attack found in SS316L samples was in the order of 1–2 µm in depth. On Inconel 625 sample surface, an oxide complex formed, resisting material dissolution into the PCM. The surface morphology of tested samples remained largely unchanged after 2500 h, but the corrosion pattern changed from an initially localized corrosion penetration to a more uniform type. After 2500 h, the corrosion depth of Inconel 625 remained at roughly 1–2 µm, indicating that the corrosion rate decelerated. Both materials demonstrated good compatibility with the chosen NaF–NaCl eutectic salt, but the low corrosion activity in Inconel 625 samples shows a performance advantage for long term operation.

**Keywords:** thermal energy storage (TES); phase change material (PCM); concentrating solar power (CSP); molten salt; material compatibility; corrosion rate

## 1. Introduction

One of the main challenges limiting the widespread implementation of solar and wind energies for grid-scale electricity generation is the transient nature of the renewable energy resources. One promising technology is solar thermal power generation because surplus solar radiation can be stored directly as thermal energy without costly conversion losses. Thermal energy storage (TES) has been implemented at operational concentrating solar power (CSP) plants using the sensible heat of a large amount of molten salt [1–3]. These systems require complex pumping systems, large storage mass volumes for megawatt power generation, a high degree of insulation to prevent the molten salt from solidifying, and they have a low solar to electric efficiency of only 15 to 20 percent. A latent heat-based TES system vastly reduces the overall size and thus the cost of storage systems by utilizing the vast amount of energy required to change a material's state. The reasonably high heat of fusion and relatively small volumetric change of solid-liquid phase transition in comparison to solid-solid and liquid-gas transitions make it well suited for various TES applications. Numerous materials have been investigated as potential phase change materials (PCM) over a wide range of temperatures including paraffin wax, fatty acids, NaNO<sub>3</sub>, KNO<sub>3</sub>, NaNO<sub>3</sub>–KNO<sub>3</sub> eutectics, NaCl, and sodium borate oxides [1,4–6]. Ushak et al. [7] and Gomez et al. [8] reviewed the appropriate usage of some molten

salts along with other storage media in TES systems including Hitec solar salt, mineral oil, synthetic oil, silicone oil, nitrate salts, carbonate salts, and liquid sodium. However, most of the studied materials had a low solid thermal conductivity which vastly reduces the heat transfer rate during solidification. Research into various means of increasing the heat transfer rate is a wide topic that includes embedding a highly conductive material into the PCM [9–14], encapsulation [4,5,15–22], embedding fins into the PCM [23–25], and using heat pipes [26–35].

In the development of a TES system, one of the major challenges is the appropriate selection of materials for the construction of the salt container. Key requirements include strength and corrosion resistance at elevated temperatures, raw material cost, commercial availability, and manufacturability using common fabrication methods. Kuravi et al. [2] provided a list of materials that are suitable for use in TES systems based on the type of PCM salt utilized and the operating temperatures. These materials include (but are not limited to) AISI 1015 carbon steel, AISI K01200, stainless steel 304, stainless steel 316, A36 carbon steel, and high nickel alloys. Zhao et al. [5] reported that there was no degradation of a MgCl-SS304 encapsulated PCM capsules after prolonged exposure to high temperatures. Zahrani and Alfantazi [36] presented their findings on the corrosion behavior of Inconel 625 in a  $\text{PbSO}_4\text{--Pb}_3\text{O}_4\text{--PbCl}_2\text{--Fe}_2\text{O}_3\text{--ZnO}$  molten salt environment. The mixture of the molten salt was tested in the air at temperatures of 600, 700, and 800 °C. They identified the following as corrosion attack modes: the formation of voids, general surface corrosion, intergranular corrosion, internal oxidation and sulfidation, and a network of distributed pores on the surface and the cross-section. Sarvghad et al. [37] conducted a compatibility study of SS 316, duplex steel 2205, and carbon steel 1008 with  $\text{NaCl--Na}_2\text{CO}_3$  at 700 °C and  $\text{Li}_2\text{CO}_3\text{--K}_2\text{CO}_3\text{--Na}_2\text{CO}_3$  at 450 °C in air for TES. Stainless steel 316 displayed the greatest resistance to corrosion due to the formation of films on its surface. At 450 °C, the corrosion mechanism for all alloys considered was uniform without localized attack. At 700 °C, oxidative attacks on grain boundaries were the primary corrosion mechanism. A review of the literature by Gil et al. [1] indicated that the corrosion rate of stainless steel is increased by approximately 25–50% during thermal cycling compared to isothermal immersion in molten nitrate salts and that the chloride content of the molten salt has an impact on the corrosion rate. The authors also state that carbon steels may be considered as potential TES containers in applications where exposure to nitrate salts can be limited to less than 400 °C. Liu et al. [38] conducted a study of isothermal corrosion of TP347H, C22 alloy, and laser-cladding C22 coating in molten alkali chloride salts in air at 450–750 °C. Gomez-Vidal and Tirawat [39] presented the results of corrosion tests for several alloys in a eutectic molten chloride solution at 650–700 °C in a nitrogen atmosphere. The alloys tested included stainless steel 310, stainless steel 347, Incoloy 800H, and Inconel 625, with Inconel 625 having the greatest corrosion resistance at  $2.80 \pm 0.38$  mm/year. Sarvghad et al. [40] examined the compatibility of Inconel 601 with  $\text{NaCl--Na}_2\text{CO}_3$  and  $\text{NaCl--Na}_2\text{SO}_4$  at 700 °C in air. They also studied the compatibility of Inconel 601 with  $\text{Li}_2\text{CO}_3\text{--K}_2\text{CO}_3\text{--Na}_2\text{CO}_3$  at 450 °C in air. It was determined that oxidation was the primary mechanism leading to oxide deposits on the oxide surface, and de-alloying was detrimental to the material to 700 °C, with the availability of oxygen controlling its rate.

The material compatibility study was conducted to determine the suitability of two metal alloys for TES vessels containing a phase-change material. The PCM used in the study was a NaF–NaCl eutectic mixture. This NaF–NaCl eutectic mixture was chosen as PCM due to (1) extremely low cost; (2) availability; (3) the melting temperature of 680 °C, which is close to the optimal operating temperature of the commercially available Stirling engine used for the project. Most of the PCM studied in the past was for an operating temperature much lower than what we were looking for. Other materials, such as liquid metals are good for a high operating temperature, but the cost is too high. The long-term testing data for this specific eutectic mixture of NaF–NaCl was not available. The closest PCM materials for high temperature TES are the ones used for NASA Solar Dynamic Space Power Systems in the 1980s [41]. NASA data was used as the guidance for our selection of the PCM and sample container materials and the testing, but no direct comparison could be made.

CSP with Dish Stirling has been explored over many years as it offers excellent prospects for mass production of low-cost, high efficiency electric power [3,42] and TES has begun to be integrated with these systems [43,44]. For a typical integrated TES/CSP system, sunlight is directed onto the TES receiver via mirrors on a parabolic dish concentrator. A heat transport device such as high-temperature heat pipes or a pump loop system is often used to transfer thermal energy to the PCM. This heat transport device also transfers heat to the Stirling engine during PCM discharge. Figure 1 shows the integrated dish Stirling CSP system with a TES module. The operating temperature of the TES module varies from local ambient to 700 °C due to solar insolation variations throughout the day. To be representative of a TES system, the test of the TES material samples was operated at 750 °C.

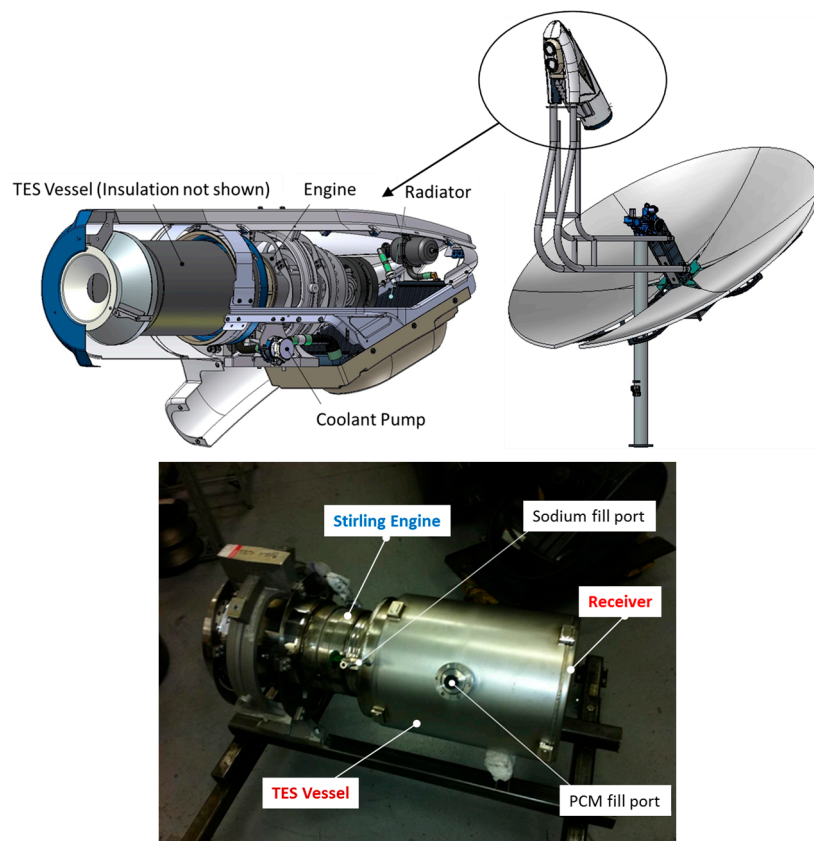


Figure 1. Integrated TES and Dish Stirling CSP.

## 2. TES Vessel Material Selection

Molten salts are used in a variety of fields including nuclear, air and space, as well as solar power generation. An extensive review of the literature was performed to evaluate the applicability for their use in a TES system. The data gathered from NASA Solar Dynamic Space Power Systems Program have the closest similarities to the current TES as they used alkali halide salt based PCM at high operating temperature. A down-select process resulted in five candidate materials for potential use as the TES container material with alkali halide salt based PCM. Of these five materials, stainless steel 316L (SS316L) and Inconel 625 were selected for testing because of their raw material cost and availability. Although numerous compatibility studies have previously been conducted with alkali fluoride salt mixtures, studies of NaF–NaCl eutectic mixtures were not found. Based on the chemical similarities of the chosen salt with those in previous studies, the previous studies were used to guide the current material section. The results of previous alkali fluoride salt material compatibility studies are summarized in the following points:

- High-temperature alloys can be used as containers for molten salt TES. Most notably, Inconel 617 and stainless steel 304 have demonstrated limited degradation with no signs of failure even after five years of thermal cycling.
- Oxygen, water residue, and sodium cations are the three oxidizing agents present in the PCM salt system.
- Over time, the corrosion rate of the metallic alloys in a molten salt will decelerate due to the limited availability of strong oxidizing agents.
- Minimizing the levels of oxygen and water vapor inside a TES vessel is crucial to the life of the hardware. Corrosion can cause material failure in under a week if significant traces of water and oxygen are present.
- Due to low electronegativity amongst the elements present in the material, sodium cations are not expected to be an active oxidizer within the system.

Table 1 lists the alloys that were initially considered for use in the TES module. Due to high cost, lack of availability, and manufacturing difficulties, Hastelloy N, Inconel 617, and Incoloy 800HT were eliminated.

**Table 1.** TES vessel material candidates.

Candidate Material	Alloy	Ni	Fe + Cr	\$ Rank
Stainless Steel 316L	Fe–Cr	Low	High	Low
Incoloy 800HT	Ni–Fe	↓	↑	↓
Inconel 617	Ni–Cr			
Inconel 625	Ni–Cr			
Hastelloy N	Hi Ni	High	Low	High

### 3. Sample Preparation and Testing

Figure 2 shows a sample container with an interior volume of 35 mL, fabricated out of both Inconel 625 and stainless steel 316L. To avoid contamination, the end caps and a small fill tube were electron beam welded to the cylindrical body. Using the fill tube, salt was added to the container. The fill tube was crimped and sealed using fusion welding after the samples were filled.

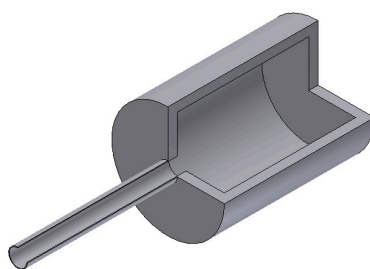


**Figure 2.** A sample container for compatibility testing.

The sample containers were first cleaned in a solvent using ultrasonic agitation and deionized water. The samples were dried using nitrogen gas and then baked-out at 200 °C for over 3 h under atmospheric conditions in an oven. After baking under atmospheric conditions, the samples were heated for 4 h at 400 °C in a vacuum furnace at  $1.6 \times 10^{-4}$  Torr. In an effort to minimize excess oxygen and water contaminants before filling the samples, the salt PCM constituents were heated to 200 °C by a hotplate in a glove box for 10 h. The sample containers were filled with a NaF–NaCl mixture at 4N grade (99.99% purity). The filling was conducted in the glove box. The volume change upon melting was accounted for when filling the samples. The container was oversized to accommodate the thermal expansion of PCM from solid to molten salt at the desired operating temperature. The PCM

was initially in powder form with very low compaction factor. The PCM filling was accomplished by taking several steps. Each time, only a portion of PCM powder was filled into the container and a band heater wrapped around the container was turned on to let PCM melt completely. The band heater was shut off after the melting to let the PCM cool down until it completely solidified to high compaction solid. This process was repeated until the container was filled with the desired amount of PCM. The filling process was conducted in a glove box. The glove box can provide environmental conditions of  $O_2 < 10$  ppm and  $H_2O < 10$  ppm. Once the samples were filled the container had the vacuum pulled down to  $10^{-6}$  Torr. A hydraulic crimping tool was used to punch the fill tube. After the punch, the fill tube was cut and fusion welded across the crimp.

Multiple samples of both Inconel 625 and stainless steel 316L were fabricated and then heated in an oven to 750 °C. The melting temperature of the NaF–NaCl eutectic salt is around 680 °C. Although the outer surfaces of the containers were exposed to ambient condition, the interior salt is under a  $10^{-6}$  Torr vacuum. The samples were held at 750 °C for 100 or 2500 h at which point they were taken out from the oven for examination.

#### 4. Test Results and Discussion

After 100 and 2500 h of heating, the Inconel 625 and stainless steel 316L samples were taken out from the furnace and then cut open. Scanning electron microscopy (SEM) and energy dispersive X-ray spectroscopy (EDX) were used to analyze the interior surface and the cross-section of the containers. Other techniques for characterizing the samples were also explored. It would be better if both the vessel materials and the PCM were examined. The dissolution of the chemical elements of the vessel materials into the PCM can be better characterized by conducting a chemical analysis on the molten salt. Additionally, examining the molten salt may further aid the study of the impact of the dissolved chemical elements on the degradation of the molten salt's performance. Note that this paper will only present the measurements and analysis results of the container materials as the focus of the project was on the container materials. The primary chemical compositions of both stainless steel 316L and Inconel 625 were measured from the same material batch used for the fabrication of the sample containers. Tables 2 and 3 present the key alloy compositions of the unheated materials.

**Table 2.** Chemical composition of SS 316L, raw material prior to fabrication.

Sample Material	C	Fe	Cr	Ni	Mo	Mn	Cu
SS 316L	0.21%	78%	16.5%	10.1%	2.05%	1.7%	0.43%

**Table 3.** Chemical composition of Inconel 625, raw material prior to fabrication.

Sample Material	C	Fe	Cr	Ni	Mo	Nb	Al
Inconel 625	0.005%	1%	20.5%	66%	8.3%	3.38%	0.21%

A sample from the side wall of the vessel that was near the end cap and the weld zone was used for SEM. The sample was mounted on the holder using carbon coated, conductive adhesive tape. A Quanta 3D FEG by FEI Corp was used for SEM analysis.

An unused sample container was used to develop a baseline for comparison and therefore was analyzed first. No corrosion was observed, as expected the surface was protected by a chromium oxide layer. However, a top surface EDX analysis revealed that there was an enrichment of manganese and copper, Table 4. Of all of the alloy constituents, manganese and copper have the highest vapor pressure at elevated temperatures [45]. Thus it is probable that the elements preferentially evaporated during the welding process and were then re-deposited on to the surface during cooling. To gain a better understanding of how the microstructure and chemical composition of the raw stainless steel 316L material were impacted by both machining and the electron beam welding process,



an in-situ ion milling process was performed using focused ion beam technology to obtain detailed information from the cross-section of the samples. First, the alloy cross-section surface was roughly milled by the ion beam and then finely polished/etched by the secondary ion beam to expose the underlying microstructural details. The surface morphology of the untested sample is shown in Figure 3. The defects seen in Figure 3 are machining marks.

**Table 4.** EDX chemical analysis and key element concentration at SS316L surface after machining and Electron Beam welding, untested.

Sample Material	O	Fe	Cr	Ni	Mn	Cu
SS 316L	1.6%	46%	18.4%	5%	23%	2%

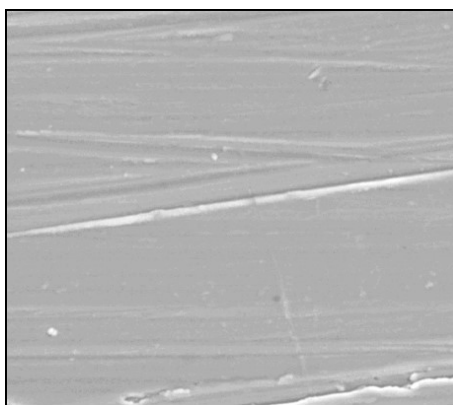


**Figure 3.** Top-down SEM image of an untested SS 316L sample surface (5000 $\times$ ).

An SEM image of the cross-section of the untested stainless steel 316L sample is presented in Figure 4. Between the sample surface and the deposited carbon protection layer, a half micron thick layer can be seen. In Figure 4, the top layer is the deposited carbon layer used to protect the material during the ion milling process. The manganese content of the layer was further confirmed by EDX analysis and a level of over 20% was measured. This further confirms that the enrichment of Mn and Cu at the surface results from the metal elements being vaporized during the electron beam welding process and were then deposited back onto the substrate.

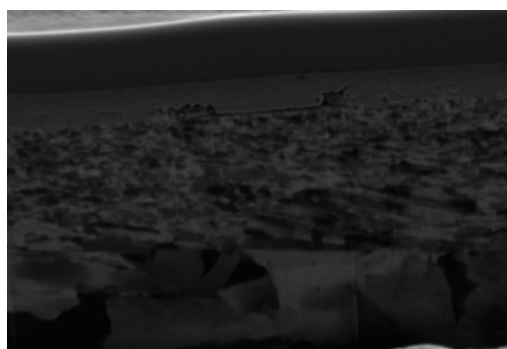


**Figure 4.** Cross-section SEM image of untested SS 316L sample, (20,000 $\times$ ).

#### 4.1. Stainless Steel 316L, 100 H Test

The interior surface of a stainless steel 316L sample after 100 h of heating is shown in Figure 5. The sample for examination was selected at a location far from the weld zone. A significant amount of

roughness can be seen on the sample's surface. Both grain boundaries and polycrystalline grains are visible. The homogeneous surface roughness and a shallow V-shaped groove on corrosion sites indicate that corrosion progressed uniformly in all directions. The least desired form of corrosion for TES applications is unidirectional corrosion penetration along a grain boundary. This type of corrosion progresses mainly in the Z direction along the grain boundary and the metal loss within the grains is insignificant. It is undesirable because even a very small amount of metal loss could reduce the material thickness significantly, resulting in early failure. This was not seen in the examined sample. The morphology seen further indicates that two localized metal dissolutions started: pitting and inter-granular. The dissolution level changes profoundly along the grain boundaries, but the majority had a very small amount of corrosion. At grain boundary junctions, the corrosion pits were also observed. This suggests that all localized attacks started at the boundaries. Lastly, corrosion products were found in the sample substrate. This indicates that dissolution of the corrosion products into the molten salt occurred via Lewis acid reaction process between the hot molten inorganic halides and the surface oxide [46,47].

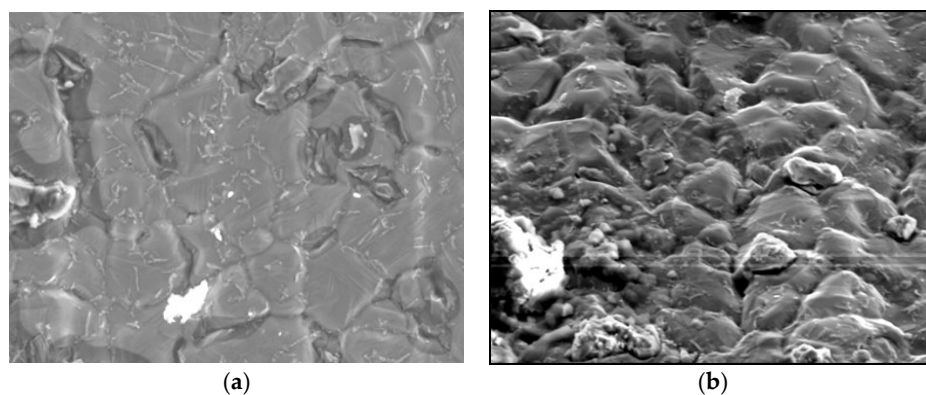


**Figure 5.** (a) Top-down and (b) tilted SEM images of SS 316L sample surface after 100 h heating (5000 $\times$ ).

Figure 6 shows the four sample surface locations selected for EDX chemical analysis. The results of the EDX analysis are presented in Table 5. The distribution of salt particles and surface oxide on the sample surface were not even. In Figure 5 the dark areas have low oxygen and sodium levels, indicating minimal to no oxide or salt present. The levels of sodium, oxygen, and fluorine were undetectable at site 1 indicating no salt and oxide in this area. Both sites 2 and 3 show a slight amount of salt and oxide. Not only does site 4 have typical salt morphology with oxygen, fluoride, and sodium concentrations over 10%, but also a chromium enriched surface oxide is present. Noteworthy is the enrichment of molybdenum at sites 1 and 2 and the manganese depletion at sites 1 to 3.

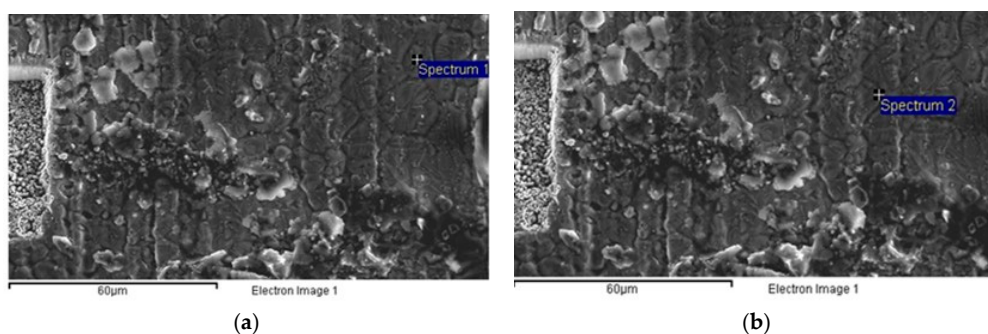


**Figure 6.** Cont.

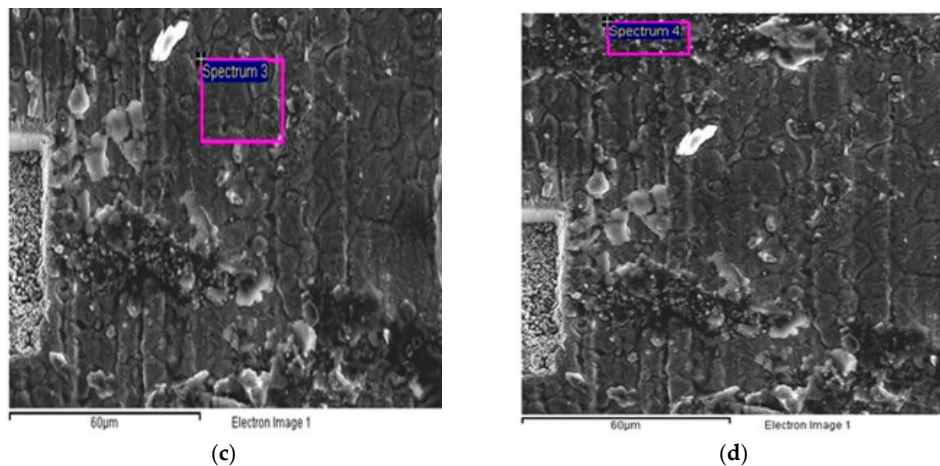


**Figure 6.** Selected sites on SS316L sample surface for EDX analysis: (a) Sample location 1; (b) Sample location 2; (c) Sample location 3; (d) Sample location 4.

**Table 5.** EDX chemical analysis, weight percentage of SS 316L sample surface after 100 h testing.

Sample Site	O%	F%	Na%	Fe%	Cr%	Ni%	Mo%	Mn%
1	-	-	-	71	11.62	10.9	6	-
2	2.55	-	-	61	10.54	8.7	10.2	-
3	1.78	-	1.57	70	11.24	10.3	3	-
4	11	13.4	16.7	11.5	33.06	1.6	-	2.1

Figure 7 shows a cross-section view of the sample after 100 h heating. The micro-voids resulting from element depletion were not visible. The deep grain boundary corrosion penetration was not present. As a result of annealing, grain recrystallization and growth occurred replacing the refined and highly distorted grains seen in the untested sample. This is desirable because the larger annealed grains are more stable and thus provide a higher resistance to corrosion than that of the grains that are plastically deformed.

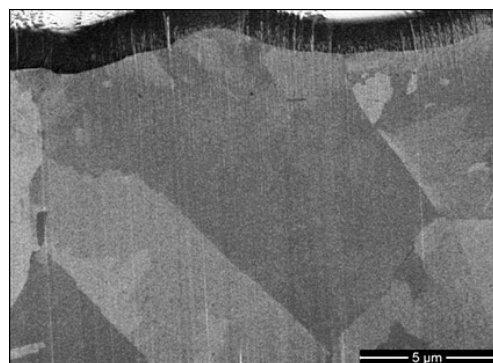


**Figure 7.** Cross section SEM image (12,000×).

The cross section of the 100 h stainless steel 316L sample was analyzed with EDX to characterize the key elements concentration. Performing EDX on the cross section provides better information than that done on the surface because the surface oxide and salt contamination are reduced. The locations where EDX was performed are shown in Figure 8 while the results are presented in Figure 9. The variation in the concentrations of nickel and iron were unremarkable. Additionally, molybdenum enrichment and surface chromium depletion were evident. The primary corrosion mechanism of stainless steel is chromium dissolution. At a depth of roughly 6 microns, nominal composition was observed.



The chromium dissolution to the salt occurred in two reaction paths. First, the reaction of chromium with oxidants from any remaining  $O_2$  or  $H_2O$  resulted in the formation of chromium oxide on the surface which dissolved into the molten salt. Second, the precipitation of chromium carbide at the grain boundaries dissolved into the molten salt. This molybdenum enrichment is in contrast to the near surface chromium reduction. At elevated temperature, high diffusion mobility of the chromium results in its depletion. The vacancies resulted from the chromium depletion drive the molybdenum to the surface [48]. Additionally, at elevated temperatures the migration of molybdenum to the grain boundaries resulted in the formation of carbides.

The last area that was examined was the weld zone. In an effort to avoid introducing contaminants into the sample, electron beam welding was used during fabrication. However, the composition, microstructure, and properties of the material were changed by the welding process. Figure 10 shows a cross-section of the weld zone from the 100 h stainless steel 316L sample. A few micron thick layer can be seen at the top of the image. This layer was formed due to metal overflow from the fusion pool. A coating from metal vapor deposition can also be seen in Figure 10. The vertical lines seen resulted from the rough ion beam milling process during the preparation of the sample. Between the upper layer and the base material, an interface layer was formed indicating that the fusion was incomplete. Additionally, micro-voids are present both along and adjacent to the boundary.

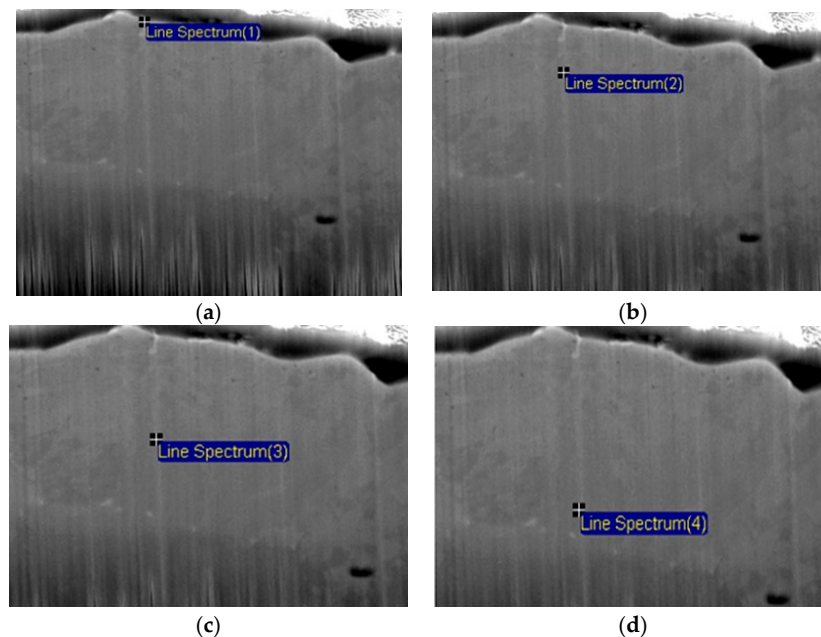


**Figure 8.** Selected locations over substrate cross section for EDX analysis: (a) Sample location 1; (b) Sample location 2; (c) Sample location 3; (d) Sample location 4.

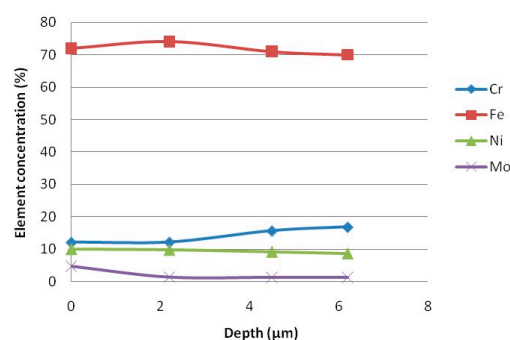


**Figure 9.** EDX chemical analysis of SS 316L sample after 100 h heating.

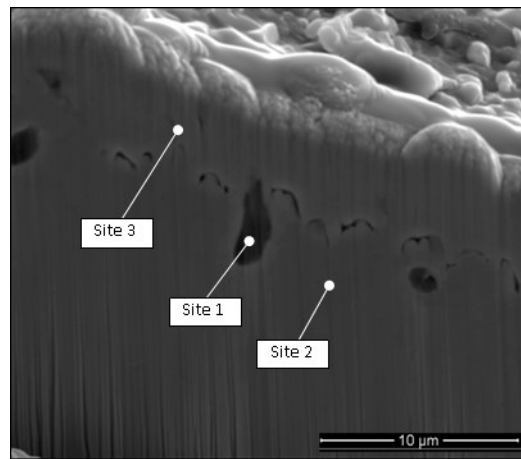


**Figure 10.** Cross-section SEM image of SS 316L sample in the weld zone after 100 h heating.

Three locations on the cross-section were chosen for EDX analysis. These areas were labeled as 1 for the largest void at the center, 2 for the base material, and 3 for the top layer, respectively. The results of the EDX analysis are listed in Table 6. At site 1, the presence of the salt is evident by a large fraction of sodium and chlorine present within the void area. It is possible that the salt could have fallen into the void from the surface during the ion beam milling process. It is also possible that the void area was connected via a grain boundary or micro-crack to the surface in contact with the salt due to the melding process. Manganese depletion was also evident at all three sample sites. This further suggests that at high vapor pressure, the element evaporated during the welding process and later redeposited on the surface during cooling.

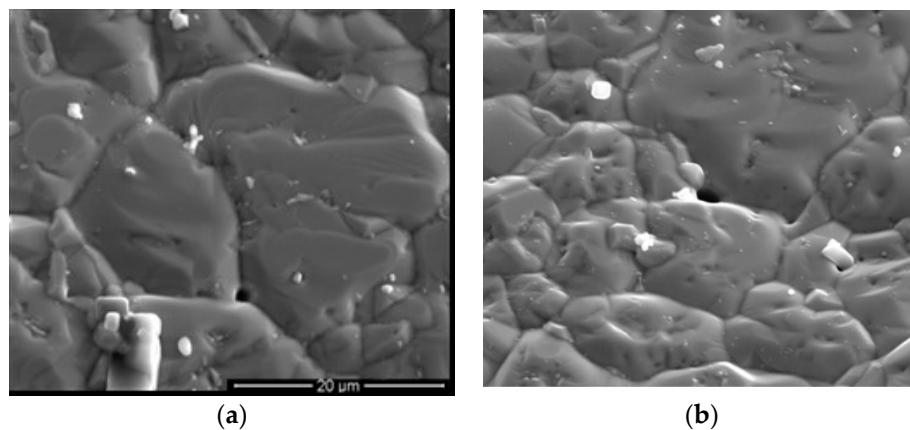
**Table 6.** EDX chemical analysis and resulting weight percentage of SS 316L sample in the weld zone, 100 h testing.

Sample Site	O%	Cl%	Na%	Fe%	Cr%	Ni%	Mo%	Mn%
1	1.7	20.5	10.5	50	15.2	9.6	1.6	0.5
2	1.1	-	-	70.1	17.1	8.7	1.5	1.0
3	1.4	0.3	1.57	71	11.24	9.1	3	0.7

Immediately after the stainless steel 316L sample was cut open, the color of the eutectic salt was visually inspected and its appearance was a pure white color. This also suggests that minimum corrosion had occurred. The color of a halide salt is sensitive to the level of chromium dissolution. It has previously been reported that salt discoloration from white to yellow can occur even after a 100-h reaction of the halide salt in a pre-baked stainless steel capsule [46]. To confirm the high sensitivity of the change in salt color, a simple re-melting test of the used NaF–NaCl eutectic salt mixture was conducted during which the top cap of the sample was removed leaving the interior of the stainless steel 316L sample and the salt exposed to the ambient environment. When the container was not sealed, the color of the eutectic salt changed from pure white to a light yellow after only one cycle of solidification and re-melting.

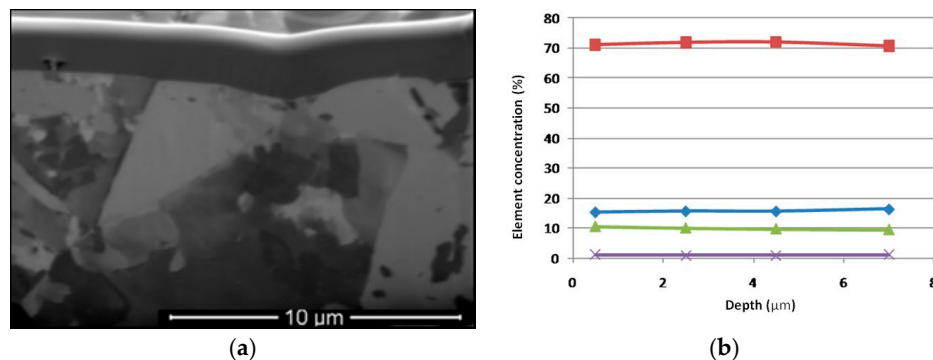
#### 4.2. SS 316L, 2500 H

Figure 11 shows that surface morphology of a sample after 2500 h of heating. The results indicate that a uniform metal dissolution process occurred at some point after the initial 100 h. While there were no signs that profound intergranular corrosion occurred, more pits presented at the junctions of grain boundary while shallow pits were observed within the grains themselves. Preferential dissolution occurred along certain crystal orientations as some grain facets were exposed. The noted characterizations suggest that a change in the corrosion mechanism occurred between 100 and 2500 h' exposure with the molten salt. The corrosion became uniform on a macro-scale after an initial intergranular boundary attack.



**Figure 11.** (a) Top-down and (b) 20° tilted SEM images of SS 316L sample surface, 2500 h testing (5000×).

The conclusions that no intergranular penetration occurred can be substantiated by examining the increased resolution image of the cross-sectional area shown in Figure 12a. Instead of the top down surface EDX analysis that was done on the 100 h sample, a more accurate cross-section survey was performed. The results are presented in Figure 12b. The concentrations of the key elements were compared to those seen in the 100 h samples. The variation in the concentration of the key elements with the sample's depth is less since the elements had sufficient time to migrate to their respective equilibrium concentrations within the material.



**Figure 12.** (a) Cross section SEM image (10,000×) and (b) EDX chemical analysis of SS 316L sample after 2500 h heating.

As with the 100 h sample, the weld zone cross section was also analyzed via SEM. Unlike in the 100 h heated sample, the distinct fusion pool layer and micro-voids in the weld zone were not present in the 2500 h sample. The exact cause for this is unknown. A plausible explanation is that corrosion occurred at the interface boundary between the fusion pool and the base metal layers. This would allow the thin fusion pool layer to delaminate from the material surface.

#### 4.3. Inconel 625, 100 H

As with the stainless steel 316L samples, an untested Inconel 625 sample was examined as a baseline for comparison. Similar to the results of the stainless steel 316L sample, the cold work introduced grain refinement and distortion as well as machining marks being visible in both images of Figure 13. However, unlike with the stainless steel 316L, the EDX analysis results showed that no surface elements deviated from the nominal composition of the bulk alloy. Although the same equipment and process parameters were used for the electron beam welding of both the Inconel 625 and stainless steel 316L containers,

manganese and copper enriched thin film were not found in the Inconel sample. Inconel 625 has elements of a low vapor pressure and high melting temperature. The manganese and copper content of Inconel are 0.03% and 0.02% respectively. These levels are at least an order of magnitude lower than that of stainless steel 316L, thus during the welding process, there were insufficient elements with high vapor pressure to evaporate and then redeposit during cooling. The chemical composition of the Inconel 625 surface after the welding process is shown in Table 7.

Comparing to the stainless steel 316L sample, the images of the Inconel 625 sample surface were significantly different after 100 h of heating. The surface of the Inconel 625 sample was covered evenly by both salt residues and oxide. Ultrasonic agitation was employed to clean the sample in a de-ionized water bath to aid in the evaluation of the samples. The sample surface after cleaning is shown in Figure 14. A 0.5  $\mu\text{m}$  thick oxide layer uniformly covered the surface, Figure 15. The formation of the oxide layer starts as a grain with the size of a few hundred nm and then agglomerates and forms a dense layer. However, gaps are present among the grains which permit the molten salt intrusion.

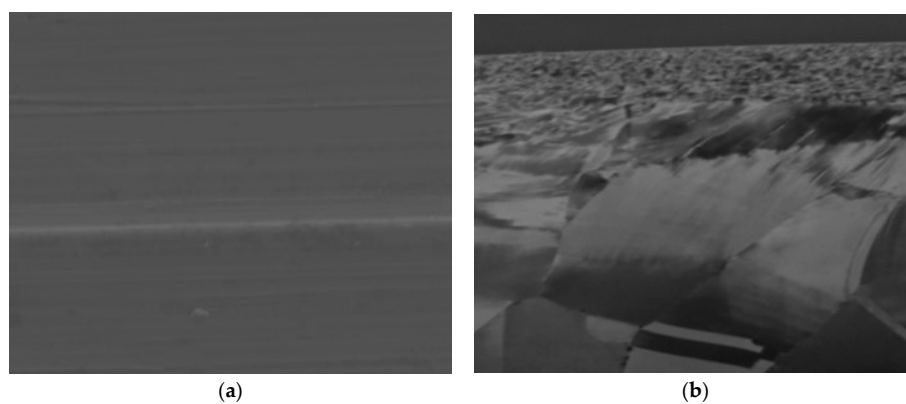


**Figure 13.** (a) Top down and (b) cross sectional SEM images of Inconel 625 sample surface, prior to test (5000 $\times$ ).

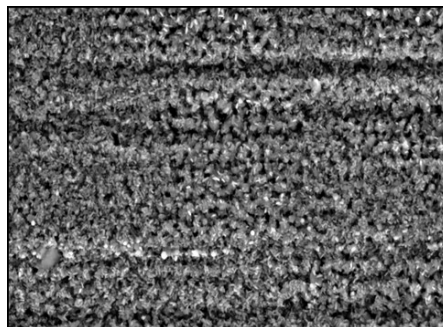


**Figure 14.** Top-down SEM image of Inconel 625 sample surface after 100 h heating (5000 $\times$ ).

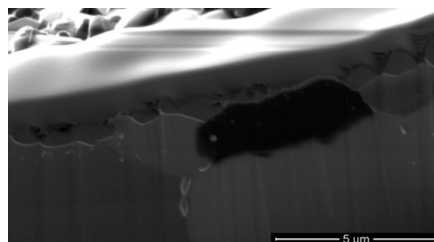


**Figure 15.** SEM image of oxide complex formed on the Inconel 625 surface. The top layer is shown on Image is a carbon coat protection layer for the ion milling process (20,000 $\times$ ).

**Table 7.** Chemical composition at Inconel 625 surface after machining and EB welding, untested.

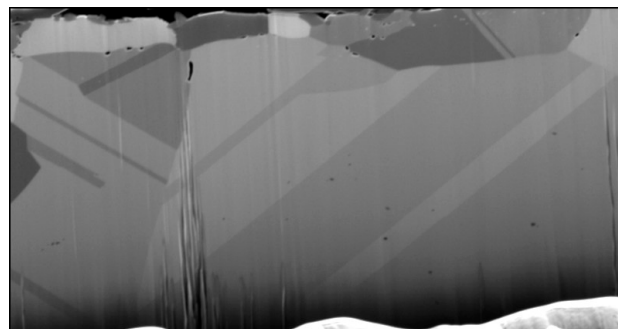
Sample Material	O%	Fe%	Cr%	Ni%	Mo%	Nb%	Al%
Inconel 625	0.47	1.6	20.7	65.4	8.4	3.2	0.3

The oxide complex that forms on the surface of the Inconel 625 sample is stable and resistant to dissolution, unlike the oxide that forms in the stainless steel 316 L samples which is easily dissolved in the molten salt. An EDX analysis of the surface was conducted on a single location and the results are listed in Table 8. Note that the values in Table 8 are listed in atomic percentage. The exact oxide could not be determined based on the EDX analysis alone, however, the oxide is rich in nickel and chromium. The extremely low Na and Mo contents indicate minimal interaction with both the salt and the alloy substrate.

**Table 8.** The atomic percentage of Inconel 625 sample surface after 100 h testing.

Element	Cr	O	Ni	Mo	Fe	Na
Atomic%	49	31	21.5	1.5	0.6	0.25

A view of the microstructure of the Inconel 615 sample's cross-section can be seen in Figure 16. The grains along the top surface are much smaller than those seen deeper in the sample. Additionally, recrystallization formed annealing twins were found in the large grains. After 100 h of heating, it appears that the majority of the grains have undergone recrystallization. The recrystallization of grains reduces grain boundary migration mobility. Low grain boundary mobility decreases both growth and recrystallization in the annealing process. Furthermore, when carbides are formed on grain boundaries they have a pinning or retarding effect on the mobility of the grain boundary and therefore slows down the recrystallization and the growth [49].

**Figure 16.** Cross-sectional SEM image of Inconel 625 sample after 100 h heating (10,000×).

A total of four sites were selected for the EDX analysis on the cross-section. The first site, site 1, was chosen in the oxide layer. Sites 2 and 3 were picked at grain boundaries and precipitates. Site 4 was selected within the sample base material. The results of EDX analysis are tabulated in Table 9. The surface analysis results from site 1 further substantiate the presence of a chromium enriched oxide. Aluminum oxide precipitates are present based on the results from sites 2 and 3. As expected the results from site 4 are comparable to the untested baseline composition. Note that sodium from the eutectic salt was not observed in any of the four selected sites.

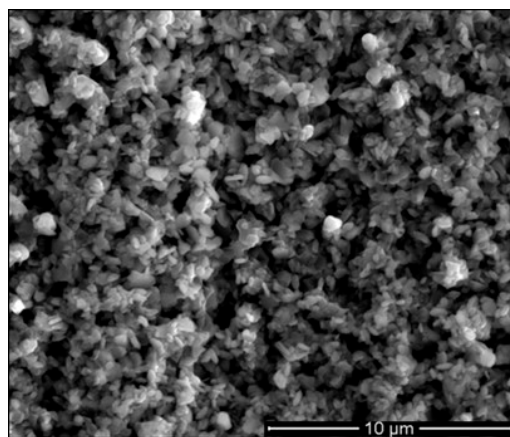


**Table 9.** The weight percentage of Inconel 625 sample cross section after 100 h heating.

Sample Site	Cr%	Ni%	O%	Mo%	Fe%	Al%	Mn%	Na%	Cl%
1	53.2	31.7	12.9	2.8	1	-	-	-	-
2	18	67.9	3.9	4.4	1.7	4.4	0.1	-	-
3	18.6	68	3.7	4.6	1.7	3.1	0.16	-	0.2
4	18.2	74.6	0.35	5.1	1.7	-	0.1	-	-

#### 4.4. Inconel 625, 2500 H

As with the 100 h sample, the Inconel sample was analyzed after 2500 h exposure to the molten salt. The Inconel 625 was also cleaned to remove any salt residue before conducting the SEM analysis. A surface morphology that was highly similar to that observed in the 100 h sample was seen in the 2500 h sample, Figure 17. The oxide layer with porous polycrystalline was still seen, but the grain size of the layer and the thickness remained unchanged. These results indicate that the formed oxide complex is resistant to container material dissolution into the eutectic mixture of NaCl–NaF used in the experiments. The porous oxide layer after 2500 h is a result of extremely slow solid-state inter-granular diffusion of the oxide under the test conditions. The temperatures present in the experiment were far below the melting point of the normal oxide.

**Figure 17.** Top-down SEM image of Inconel 625 sample surface after 2500 h heating (10,000×).

The results of a cross sections SEM analysis further validate the findings obtained from the surface analysis, Figure 18. The measured thickness of the oxide layer and the size of the grains show little change with the testing time. It was also observed that there was no apparent corrosion between the alloy surface and the oxide layer. Furthermore, there was minimal intergranular boundary attack present. A previous study reported that inter-granular grain boundary corrosion was the primary corrosion mechanism of nickel alloys in alkali halide molten salt systems [50]. Contrary to the previous report, no significant inter-granular penetration was observed in any of the samples examined. A few micron or sub-micron sized voids were seen. These are likely the result of corrosion resulting from material defects in the manufacturing process. Given the minimal change of the oxide morphology, the lack of oxide growth and the clear interface present between the oxide and the Inconel 625 alloy surface strongly supports the conclusion that, after the initial stage, the corrosion rate in the Inconel system has been greatly reduced.

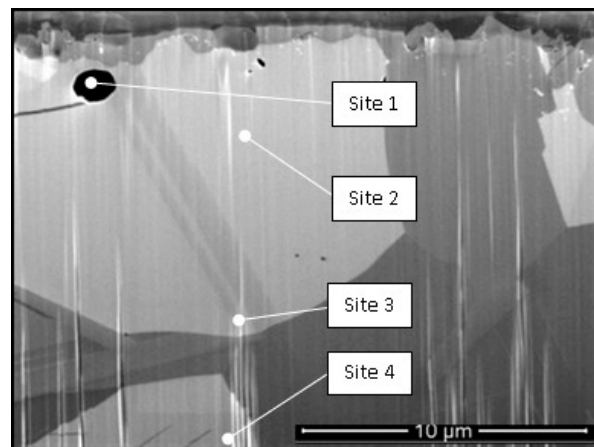


**Figure 18.** Cross-section SEM image of Inconel 625 sample after 2500 h heating (10,000×).

Figure 18 shows where the four sites for EDX analysis were chosen. As shown on the upper left corner of Figure 18, site 1 was inside the void. The other sites were located successively deeper into the depth of the cross-section towards the base alloy material. The results of the EDX analysis are listed in Table 10. The results are mostly comparable to the composition of the base alloy elements. The composition was fairly uniform across the sample with the exception of the indication of an oxide precipitate at site 2. The results from site 1 show that molten salt was able to penetrate into the void space through a grain boundary.

**Table 10.** The weight percentage of Inconel 625 sample cross section after 2500 h heating.

Sample Site	Ni%	Cr%	Fe%	Mo%	Nb%	O%	Na%	Cl%
1	64.6	19.1	1.4	2.4	0.4	0.43	7	3.7
2	72.7	18.4	1.5	5.6	1.2	30.57	-	-
3	71.5	20.7	1.3	5.2	1.2	3.7	-	0.2
4	71	19.1	1.4	5.1	1.2	0.35	-	-

## 5. Conclusions

The compatibility of stainless steel 316L and Inconel 625 to NaCl–NaF eutectic mixture was studied to determine the suitability for use in a latent heat TES system. A small amount of corrosion was present in both container materials after 100 h of high-temperature heating. However, neither sample suffered significant damage after 2500 h of high-temperature heating. The undesirable inter-granular grain boundary attack found in SS316L samples is in the order of 1–2 μm in depth. On the surface of the Inconel 625 sample, an oxide complex formed. This oxide complex is resistant to container material dissolution into the molten salt. After 2500 h of high-temperature exposure, the surface morphology of both stainless steel 316L and Inconel 625 remained largely unchanged, but the corrosion process switched from an initially localized pattern to a more uniform pattern. After 2500 h of high-temperature heating, the measured corrosion depth of Inconel 625 remained roughly 1–2 μm, indicating the deceleration of corrosion rate. Both Inconel 625 and stainless steel 316L demonstrated good compatibility with the chosen eutectic mixture of NaF–NaCl in a system that has been sealed and the excess water and oxygen inside the container has been removed. The low corrosion activity in Inconel 625 samples shows an advantage over the stainless steel 316L for long term operation. Therefore, the results can also provide good insight on the selection of the material for use in a TES system that utilizes a NaF–NaCl eutectic as PCM.

**Acknowledgments:** This work was supported by DOE EERE under the grant DE-FC36-08GO18157. The authors would like to thank Bruce Arey at Environmental Molecular Sciences Laboratory at Pacific Northwest National Laboratory (PNNL) and Brian Iverson at Sandia National Laboratory for technical support.

**Author Contributions:** Songgang Qiu served as the principal Investigator for the research project. He conceived and performed the analytical analysis. Ming Fan designed and performed experimental testing. Songgang Qiu, Ming Fan, and Laura Solomon analyzed the data and wrote the paper.

**Conflicts of Interest:** The authors declare no conflict of interest.

## Abbreviations

CSP	Concentrating Solar Power
EDX	Energy-Dispersive X-ray Spectroscopy
PCM	Phase Change Material
SEM	Scanning Electron Microscopy
TES	Thermal Energy Storage
EDX	Energy Dispersive X-ray Spectroscopy

## References

1. Gil, A.; Medrano, M.; Martorell, I.; Lázaro, A.; Dolado, P.; Zalba, B.; Cabeza, L.F. State of the art on high temperature thermal energy storage for power generation. Part 1—Concepts, materials and modellization. *Renew. Sustain. Energy Rev.* **2010**, *14*, 31–55. [\[CrossRef\]](#)
2. Kuravi, S.; Trahan, J.; Goswami, Y.; Rahman, M.M.; Stefanakos, E.K.; Goswami, D.Y.; Rahman, M.M.; Stefanakos, E.K.; Goswami, Y.; Rahman, M.M.; et al. Thermal energy storage technologies and systems for concentrating solar power plants. *Prog. Energy Combust. Sci.* **2013**, *39*, 285–319. [\[CrossRef\]](#)
3. Stine, W.B.; Diver, R.B. *A Compendium of Solar Dish/Stirling Technology*; Sandia National Laboratories: Albuquerque, NM, USA, 1994.
4. Zheng, Y.; Zhao, W.; Sabol, J.C.; Tuzla, K.; Neti, S.; Oztekin, A.; Chen, J.C. Encapsulated phase change materials for energy storage—Characterization by calorimetry. *Sol. Energy* **2013**, *87*, 117–126. [\[CrossRef\]](#)
5. Zhao, W.; Zheng, Y.; Sabol, J.C.; Tuzla, K.; Neti, S.; Oztekin, A.; Chen, J.C. High temperature calorimetry and use of magnesium chloride for thermal energy storage. *Renew. Energy* **2013**, *50*, 988–993. [\[CrossRef\]](#)
6. Solomon, L.; Oztekin, A.; Neti, S.; Jain, H.; Pfeifer, T.; Matyáš, J.; Balaya, P.; Singh, D.; Wei, J. Determination of Parameters for Improved Efficiency in Thermal Energy Storage Using Encapsulated Phase Change Materials. In *Ceramics for Energy Conversion, Storage, and Distribution Systems*; Pfeifer, T., Matyas, J., Balaya, P., Wei, J., Singh, D., Eds.; John Wiley & Sons, Inc.: Hoboken, NJ, USA, 2016; pp. 219–226. ISBN 9781119234531.
7. Ushak, S.; Grageda, M. *Using Molten Salts and Other Liquid Sensible Storage Media in Thermal Energy Storage (TES) Systems*; Woodhead Publishing Limited: Sawston/Cambridge, UK, 2015; ISBN 9781782420965.
8. Gomez, J.; Glatzmaier, G.C.; Starace, A.; Turchi, C.; Ortega, J. High Temperature Phase Change Materials for Thermal Energy Storage Applications Preprint. In Proceedings of the SolarPACES 2011, Granada, Spain, 20–23 September 2011.
9. Singh, D.; Zhao, W.; Yu, W.; France, D.M.; Kim, T. Analysis of a graphite foam-NaCl latent heat storage system for supercritical CO<sub>2</sub> power cycles for concentrated solar power. *Sol. Energy* **2015**, *118*, 232–242. [\[CrossRef\]](#)
10. Thapa, S.; Chukwu, S.; Khaliq, A.; Weiss, L. Fabrication and analysis of small-scale thermal energy storage with conductivity enhancement. *Energy Convers. Manag.* **2014**, *79*, 161–170. [\[CrossRef\]](#)
11. Almajali, M.; Lafdi, K.; Prodhomme, P.H. Effect of copper coating on infiltrated PCM/foam. *Energy Convers. Manag.* **2013**, *66*, 336–342. [\[CrossRef\]](#)
12. Kim, T.; France, D.M.; Yu, W.; Zhao, W.; Singh, D. Heat transfer analysis of a latent heat thermal energy storage system using graphite foam for concentrated solar power. *Sol. Energy* **2014**, *103*, 438–447. [\[CrossRef\]](#)
13. Zhao, C.Y.; Wu, Z.G. Heat transfer enhancement of high temperature thermal energy storage using metal foams and expanded graphite. *Sol. Energy Mater. Sol. Cells* **2011**, *95*, 636–643. [\[CrossRef\]](#)
14. Baby, R.; Balaji, C. Experimental investigations on thermal performance enhancement and effect of orientation on porous matrix filled PCM based heat sink. *Int. Commun. Heat Mass Transf.* **2013**, *46*, 27–30. [\[CrossRef\]](#)

15. Alam, T.E.; Dhau, J.S.; Goswami, D.Y.; Stefanakos, E. Macroencapsulation and characterization of phase change materials for latent heat thermal energy storage systems. *Appl. Energy* **2015**, *154*, 92–101. [\[CrossRef\]](#)
16. Jacob, R.; Bruno, F. Review on shell materials used in the encapsulation of phase change materials for high temperature thermal energy storage. *Renew. Sustain. Energy Rev.* **2015**, *48*, 79–87. [\[CrossRef\]](#)
17. Xu, B.; Li, P.; Chan, C. Application of phase change materials for thermal energy storage in concentrated solar thermal power plants: A review to recent developments. *Appl. Energy* **2015**, *160*, 286–307. [\[CrossRef\]](#)
18. Solomon, L.; Elmozughhi, A.F.; Neti, S.; Oztekin, A. High temperature thermal energy storage using EPCM-The effect of void. In Proceedings of the ASME International Mechanical Engineering Congress and Exposition (IMECE), Montreal, QC, Canada, 14–20 November 2014; Volume 6B.
19. Solomon, L.; Oztekin, A. Encapsulated Phase Change Materials for use in High Temperature Thermal Energy Storage Encapsulated Phase Change Materials for use in High Temperature Thermal Energy Storage. In *Advances in Energy Research*; Acosta, M.J., Ed.; Nova Science Publishers Inc.: Hauppauge, NY, USA, 2016; ISBN 978-1-63485-515-0.
20. Zheng, Y.; Barton, J.L.; Tuzla, K.; Chen, J.C.; Neti, S.; Oztekin, A.; Misiolek, W.Z. Experimental and computational study of thermal energy storage with encapsulated  $\text{NaNO}_3$  for high temperature applications. *Sol. Energy* **2015**, *115*, 180–194. [\[CrossRef\]](#)
21. Elmozughhi, A.F.; Solomon, L.; Oztekin, A.; Neti, S. Encapsulated phase change material for high temperature thermal energy storage—Heat transfer analysis. *Int. J. Heat Mass Transf.* **2014**, *78*, 1135–1144. [\[CrossRef\]](#)
22. Solomon, L.; Elmozughhi, A.F.; Oztekin, A.; Neti, S. Effect of internal void placement on the heat transfer performance—Encapsulated phase change material for energy storage. *Renew. Energy* **2015**, *78*, 438–447. [\[CrossRef\]](#)
23. Liu, M.; Saman, W.; Bruno, F. Review on storage materials and thermal performance enhancement techniques for high temperature phase change thermal storage systems. *Renew. Sustain. Energy Rev.* **2012**, *16*, 2118–2132. [\[CrossRef\]](#)
24. Sharifi, N.; Bergman, T.L.; Faghri, A. Enhancement of PCM melting in enclosures with horizontally-finned internal surfaces. *Int. J. Heat Mass Transf.* **2011**, *54*, 4182–4192. [\[CrossRef\]](#)
25. Hosseini, M.J.; Ranjbar, A.A.; Rahimi, M.; Bahrampoury, R. Experimental and numerical evaluation of longitudinally finned latent heat thermal storage systems. *Energy Build.* **2015**, *99*, 263–272. [\[CrossRef\]](#)
26. Shabgard, H.; Allen, M.J.; Sharifi, N.; Benn, S.P.; Faghri, A.; Bergman, T.L. Heat pipe heat exchangers and heat sinks: Opportunities, challenges, applications, analysis, and state of the art. *Int. J. Heat Mass Transf.* **2015**, *89*, 138–158. [\[CrossRef\]](#)
27. Naghavi, M.S.; Ong, K.S.; Mehrali, M.; Badruddin, I.A.; Metselaar, H.S.C. A state-of-the-art review on hybrid heat pipe latent heat storage systems. *Energy Convers. Manag.* **2015**, *105*, 1178–1204. [\[CrossRef\]](#)
28. Sharifi, N.; Wang, S.; Bergman, T.L.; Faghri, A. Heat pipe-assisted melting of a phase change material. *Int. J. Heat Mass Transf.* **2012**, *55*, 3458–3469. [\[CrossRef\]](#)
29. Motahar, S.; Khodabandeh, R. Experimental study on the melting and solidification of a phase change material enhanced by heat pipe. *Int. Commun. Heat Mass Transf.* **2016**, *73*, 1–6. [\[CrossRef\]](#)
30. Tiari, S.; Qiu, S.; Mahdavi, M. Numerical study of finned heat pipe-assisted thermal energy storage system with high temperature phase change material. *Energy Convers. Manag.* **2015**, *89*, 833–842. [\[CrossRef\]](#)
31. Tiari, S.; Qiu, S. Three-dimensional simulation of high temperature latent heat thermal energy storage system assisted by finned heat pipes. *Energy Convers. Manag.* **2015**, *105*, 260–271. [\[CrossRef\]](#)
32. Tiari, S.; Qiu, S.; Mahdavi, M. Discharging Process of a Finned Heat Pipe-assisted Thermal Energy Storage System with High Temperature Phase Change Material. *Energy Convers. Manag.* **2016**, *118*, 426–437. [\[CrossRef\]](#)
33. Mahdavi, M.; Qiu, S. Mathematical modeling and analysis of steady state performance of a heat pipe network. *Appl. Therm. Eng.* **2015**, *91*, 556–573. [\[CrossRef\]](#)
34. Mahdavi, M.; Qiu, S.; Tiari, S. Improvement of a novel heat pipe network designed for latent heat thermal energy storage systems. *Appl. Therm. Eng.* **2016**, *108*, 878–892. [\[CrossRef\]](#)
35. Mahdavi, M.; Qiu, S.; Tiari, S. Numerical investigation of hydrodynamics and thermal performance of a specially configured heat pipe for high-temperature thermal energy storage systems. *Appl. Therm. Eng.* **2015**, *81*, 325–337. [\[CrossRef\]](#)
36. Mohammadi Zahrani, E.; Alfantazi, A.M. Molten salt induced corrosion of Inconel 625 superalloy in  $\text{PbSO}_4$ – $\text{Pb}_3\text{O}_4$ – $\text{PbCl}_2$ – $\text{Fe}_2\text{O}_3$ – $\text{ZnO}$  environment. *Corros. Sci.* **2012**, *65*, 340–359. [\[CrossRef\]](#)

37. Sarvghad, M.; Steinberg, T.A.; Will, G. Corrosion of steel alloys in eutectic NaCl + Na<sub>2</sub>CO<sub>3</sub> at 700 °C and Li<sub>2</sub>CO<sub>3</sub> + K<sub>2</sub>CO<sub>3</sub> + Na<sub>2</sub>CO<sub>3</sub> at 450 °C for thermal energy storage. *Sol. Energy Mater. Sol. Cells* **2017**, *170*, 48–59. [[CrossRef](#)]
38. Liu, S.; Liu, Z.; Wang, Y.; Tang, J. A comparative study on the high temperature corrosion of TP347H stainless steel, C22 alloy and laser-cladding C22 coating in molten chloride salts. *Corros. Sci.* **2014**, *83*, 396–408. [[CrossRef](#)]
39. Gomez-Vidal, J.C.; Tirawat, R. Corrosion of alloys in a chloride molten salt (NaCl–LiCl) for solar thermal technologies. *Sol. Energy Mater. Sol. Cells* **2016**, *157*, 234–244. [[CrossRef](#)]
40. Sarvghad, M.; Will, G.; Steinberg, T.A. Corrosion of Inconel 601 in molten salts for thermal energy storage. *Sol. Energy Mater. Sol. Cells* **2017**, *172*, 220–229. [[CrossRef](#)]
41. Lacy, D.; Coles-Hamilton, C.; Juhasz, A. Selection of High Temperature Thermal Energy Storage Materials for Advanced Solar Dynamic Space Power Systems. In Proceedings of the Twenty-Second Intersociety Energy Conversion Engineering Conference (IECEC '87), Philadelphia, PA, USA, 10–15 August 1987.
42. Mancini, T.; Heller, P.; Butler, B.; Osborn, B.; Schiel, W.; Goldberg, V.; Buck, R.; Diver, R.; Andraka, C.; Moreno, J. Dish-Stirling Systems: An Overview of Development and Status. *J. Sol. Energy Eng.* **2003**, *125*, 135–151. [[CrossRef](#)]
43. Qiu, S.; Solomon, L.; Rinker, G. Development of an Integrated Thermal Energy Storage and Free-Piston Stirling Generator for a Concentrating Solar Power System. *Energies* **2017**, *10*, 1361. [[CrossRef](#)]
44. White, M.; Qiu, S.; Galbraith, R. Phase Change Salt Thermal Energy Storage for Dish Stirling Solar Power Systems. In Proceedings of the ASME 2013 7th International Conference on Energy Sustainability, Minneapolis, MN, USA, 14–19 July 2013. [[CrossRef](#)]
45. Lide, D.R. *CRC Handbook of Chemistry and Physics*; CRC Press: Boca Raton, FL, USA, 1998.
46. Mamantov, G.; Marassi, R. *Molten Salt Chemistry: An Introduction and Selected Applications*; Springer: Berlin, Germany, 1987; ISBN 978-94-009-3863-2.
47. Grimes, W.R. Molten-Salt Reactor Chemistry. *Nucl. Appl. Technol.* **1970**, *8*, 137–155. [[CrossRef](#)]
48. Luo, A.; Jacobson, D.L.; Ponnappan, R. Compatibility of Inconel 617R Alloy with LiF-MgF<sub>2</sub>-Kf Thermal Energy Storage Salts and Vacuum at High Temperature. *J. Mater. Eng. Perform.* **1992**, *1*, 755–761. [[CrossRef](#)]
49. Khanna, A.S. *Introduction to High Temperature Oxidation and Corrosion*; ASM International: Materials Park, OH, USA, 2002; ISBN 0-87170-762-4.
50. Dieter, G.E.; Kuhn, H.A.; Semiati, S.L. *Handbook of Workability and Process Design*; ASM International: Materials Park, OH, USA, 2003; ISBN 0-87170-778-0.



© 2018 by the authors. Licensee MDPI, Basel, Switzerland. This article is an open access article distributed under the terms and conditions of the Creative Commons Attribution (CC BY) license (<http://creativecommons.org/licenses/by/4.0/>).